Chapter 8
Experiments on Quantum Transport of Ultra-Cold Atoms in Optical Potentials

Martin C. Fischer and Mark G. Raizen

8.1 Introduction

In this chapter, we describe our experiments with ultra-cold atoms in optical potentials and show how we can address fundamental issues of time in quantum mechanics. The high degree of experimental control and the conceptual simplicity are the main advantages of our system. We start with an overview of the basic interaction of atoms and light and make the connection between atoms in optical lattices and solid state physics. While this latter connection has evolved into a major theme in physics over the past decade, at the time of this work it was still new and unexplored. After introduction of the theoretical model and the basic equations, we introduce the experimental apparatus. We then review our experiments to observe the Wannier–Stark ladder in an accelerating lattice. This system was used to study quantum tunneling where short-time non-exponential decay was first observed for an unstable quantum system. We then describe our experiments to observe the quantum Zeno and anti-Zeno effects for an unstable system that is repeatedly interrogated. We conclude this chapter with a brief outlook into the future.

8.1.1 The Interaction of Atoms and Light

The manipulation of the motional state of individual atoms with light fields was observed as early as 1930, when Frisch measured the deflection of an atomic beam with resonant light from a sodium lamp [15]. The measured deflection was caused by the recoil momentum that an atom acquires when absorbing or emitting a single

M.C. Fischer (✉)
Department of Chemistry, Duke University, Durham, NC 27708, USA,
Martin.Fischer@duke.edu

M.G. Raizen
Center for Nonlinear Dynamics and Department of Physics, The University of Texas at Austin, Austin, TX 78712, USA, raizen@physics.utexas.edu

Fischer, M.C., Raizen, M.G.: *Experiments on Quantum Transport of Ultra-Cold Atoms in Optical Potentials*. Lect. Notes Phys. **789**, 205–237 (2009)
DOI 10.1007/978-3-642-03174-8_8

photon of light. When an atom absorbs a photon from a beam of light, it acquires momentum in the direction of the light beam. Since scattered photons are emitted without preferred direction, the momentum acquired during the emission averages to zero over many cycles. This leads to a net force on the atom which is called the *spontaneous force*, or *radiation pressure*. The spontaneous force scales with the scattering rate and for large detunings falls off quadratically with the detuning Δ_{L} of the light from the atomic resonance [9]:

$$F_{\mathrm{spont}} \propto \frac{I}{\Delta_{\mathrm{L}}^2}\,, \tag{8.1}$$

where I is the laser intensity.

Another type of force is based on the coherent scattering of photons. The oscillating electric field of light can induce a dipole moment in the atom. If the induced dipole moment is in phase with the electric field, the interaction potential is lower in regions of high field and the atom will experience a force toward those regions. If it is out of phase, a force pointing away from regions of high field results. This force is called the *dipole force*. As opposed to the spontaneous force, the dipole force only falls off linearly with the detuning from the atomic resonance in the limit of large detuning [9]

$$F_{\mathrm{dipole}} \propto \frac{\nabla I}{\Delta_{\mathrm{L}}}. \tag{8.2}$$

From the scaling laws for the two types of forces it is clear that with sufficient laser intensity, the spontaneous force can be made negligibly small while still generating an appreciable dipole force. As early as 1970, Ashkin succeeded in trapping small particles with a pair of opposing, focused laser beams, making use of both types of forces. However, only the relatively recent development of laser cooling and trapping techniques have created the conditions for controlled manipulation of atoms with the dipole force alone [7]. While the laser cooling and trapping required to prepare our atomic sample utilized near-resonant light and thus both types of light forces, the optical lattices were composed of far-detuned light, so that only the dipole interaction was important.

8.1.2 Optical Lattices and the Connection to Solid State Physics

In our experiments we created a periodic optical potential by spatially overlapping two laser light beams. The periodicity of the resulting standing wave was determined by the interference pattern in the region of overlap. In the nodes of a standing wave, the electric field of the light interferes destructively and atoms at those positions are unaffected by the light. Away from the nodes, the dipole interaction causes a light-induced shift of the atomic energy levels, which is maximal at the anti-nodes. This shift of the energy levels – which is another way of describing the aforementioned

dipole force – is periodic in space. The system of a particle in a periodic potential is the textbook model of an electron in a crystal lattice and has been studied in great detail. In the 1920s Bloch arrived at the conclusion that due to the periodicity of the lattice, the eigenstates are plane waves modulated by periodic functions of position [4]. The implications of these findings on the description of transport in periodic potentials under the influence of externally applied fields are profound. Some of the resulting effects, such as Bloch oscillations and Wannier–Stark states, are treated in more detail in Sect. 8.4. Experimental verification of those predicted effects in crystal lattices, however, has been hindered by extremely short relaxation times. Electrons in a crystal lattice can scatter on impurities, dislocations, phonons, and even on other electrons. If the scattering occurs on a timescale faster than the timescale for coherent evolution of the system, coherent transport effects are destroyed. Advances in the production of very high purity superlattice structures in the 1970s allowed the experimental investigation of some of those coherent effects for the first time [31]. However, the ratio of the relaxation time to the characteristic timescale for coherent evolution in those systems was still only on the order of unity. In our system we can achieve a ratio on the order of 10^3. The relaxation time is mainly limited by spontaneous emission during the interaction, which can be made very small by detuning far from resonance. This high ratio and the ability to dynamically control the interaction potential in real time during the experiment allowed us to observe many of the coherent effects which are inaccessible in solid state systems. A more detailed comparison of the solid state and atom optics system is given in a recent overview article [38].

8.1.3 Interaction Hamiltonian

In this section, we derive the effective Hamiltonian for a two-level atom in a standing wave of far-detuned light, closely following Graham et al. [16]. The atom is assumed to have a ground state $|\mathrm{g}\rangle$ and an excited state $|\mathrm{e}\rangle$, separated in energy by $\hbar\omega_0$. For a single atom of such type in a classical light field $\mathbf{E}(\mathbf{r}, t)$, the Hamiltonian is the sum of three contributions: the kinetic energy of the center of mass, the internal energy, and the interaction energy [25]

$$H = H_{\mathrm{CM}} + H_{\mathrm{internal}} + H_{\mathrm{interaction}} \,, \tag{8.3}$$

where

$$H_{\mathrm{CM}} = \frac{p^2}{2M} \,, \tag{8.4}$$

$$H_{\mathrm{internal}} = \frac{1}{2}\hbar\omega_0\,\sigma_z, \quad \text{and} \tag{8.5}$$

$$H_{\mathrm{interaction}} = -\mathbf{d}\cdot\mathbf{E}(\mathbf{r}, t) = -\left(\langle \mathrm{e}|\mathbf{d}\cdot\mathbf{E}|\mathrm{g}\rangle\,\sigma^+ + \langle \mathrm{g}|\mathbf{d}\cdot\mathbf{E}|\mathrm{e}\rangle\,\sigma^-\right) \,. \tag{8.6}$$

The symbols $\sigma^{\pm}$ and σ_z denote the Pauli spin matrices. For a linear polarization vector $\hat{\varepsilon}$ of the light, we can define the resonant Rabi frequency as

$$\Omega = -\frac{\langle \mathrm{e}|\mathbf{d}\cdot\mathbf{E}|\mathrm{g}\rangle}{\hbar} = -\frac{\langle \mathrm{g}|\mathbf{d}\cdot\mathbf{E}|\mathrm{e}\rangle}{\hbar} = -\frac{\langle \mathrm{g}|\mathbf{d}\cdot\hat{\varepsilon}|\mathrm{e}\rangle}{\hbar}E \ , \tag{8.7}$$

where we have assumed a slow variation of the field amplitude $E(\mathbf{r}, t)$.

We create an optical lattice by overlapping two laser beams with identical linear polarization vectors $\hat{\varepsilon}$. The electric field is then of the form

$$\mathbf{E}(\mathbf{r}, t) = \frac{1}{2}\hat{\varepsilon}\left(E_1\, e^{i(\mathbf{k}_1\cdot\mathbf{r}-\omega_1 t)} + E_2\, e^{i(\mathbf{k}_2\cdot\mathbf{r}-\omega_2 t)}\right) + c.c. \tag{8.8}$$

Using this light field, we find that the interaction term is

$$H_{\text{interaction}} = \sum_{n=1,2} \hbar\frac{\Omega_n}{2}\left(\sigma^- e^{-i(\mathbf{k}_n\cdot\mathbf{r}-\omega_n t)} + \sigma^+ e^{i(\mathbf{k}_n\cdot\mathbf{r}-\omega_n t)}\right) \ , \tag{8.9}$$

where we have used the rotating wave approximation to drop the counter-rotating terms $\sigma^+ e^{+i\omega t}$ and $\sigma^- e^{-i\omega t}$ [25]. To separate the center-of-mass motion of the atoms from their internal state, we write the atomic state as

$$|\Psi(\mathbf{r}, t)\rangle = c_{\mathrm{g}}(\mathbf{r}, t)|\mathrm{g}\rangle + c_{\mathrm{e}}(\mathbf{r}, t)|\mathrm{e}\rangle \ . \tag{8.10}$$

We insert $|\Psi\rangle$ into the time-dependent Schrödinger equation with the Hamiltonian in Eq. (8.3) to obtain propagation equations for c_{g} and c_{e}. Following Graham et al. [16] for a sufficiently large detuning from resonance, we can adiabatically eliminate the excited state amplitude and remain with an equation for the (phase transformed) ground state amplitude $\tilde{c}_{\mathrm{g}}$

$$i\hbar\partial_t\tilde{c}_{\mathrm{g}} = \left[\frac{p^2}{2M} + \hbar\frac{\Omega_1\Omega_2}{4\Delta_{\mathrm{L}}}\left(e^{i(\mathbf{q}\cdot\mathbf{r}-\delta t)} + e^{-i(\mathbf{q}\cdot\mathbf{r}-\delta t)}\right)\right]\tilde{c}_{\mathrm{g}} \ , \tag{8.11}$$

where $\mathbf{q} = \mathbf{k}_2 - \mathbf{k}_1$, $\delta = \omega_2 - \omega_1$ (the frequency difference between the two beams), and $\Delta_{\mathrm{L}} = \frac{\omega_1+\omega_2}{2} - \omega_0$ (their average detuning from resonance). This leads to an effective Hamiltonian for an atom in the ground state

$$H = \frac{p^2}{2M} + V_0\cos\left(\mathbf{q}\cdot\mathbf{r} - \phi(t)\right) \ , \tag{8.12}$$

where for generality we have introduced an arbitrary time-dependent phase $\phi(t)$ (the instantaneous frequency difference is $\delta(t) = \frac{\mathrm{d}\phi}{\mathrm{d}t}$). The amplitude of the potential term is

$$V_0 = \hbar\frac{\Omega_1\Omega_2}{2\Delta_{\mathrm{L}}} \ . \tag{8.13}$$

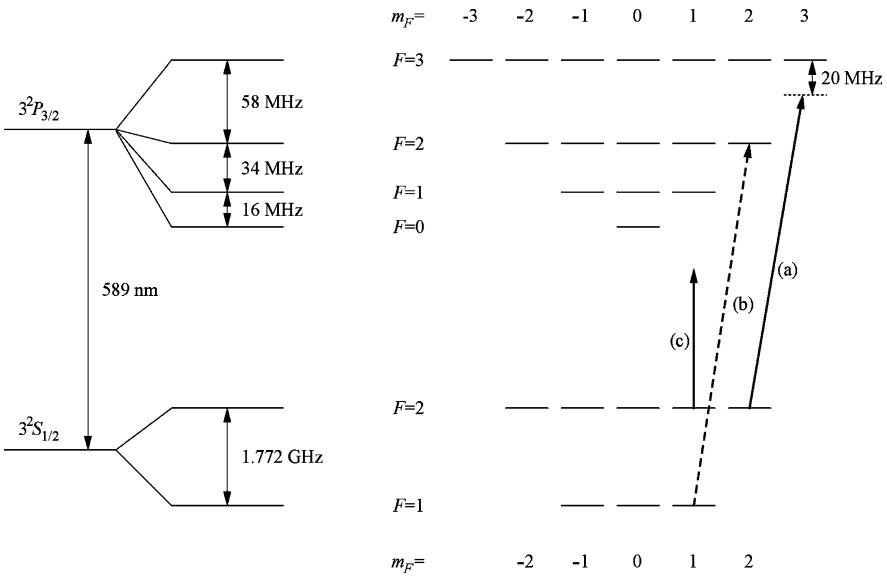

Fig. 8.1 Term diagram for the sodium D_2 line. The nuclear spin of sodium is $I = 3/2$, and so the ground state of sodium $3S_{1/2}$ has two hyperfine levels $F = 1, 2$. For the $3P_{3/2}$ excited state, we have $J = 3/2$ so that $F = 0, 1, 2, 3$. The $2F + 1$ magnetic sublevels are also shown. Representative examples of (**a**) the cooling and trapping light, (**b**) the optical pumping sideband, and (**c**) the far-detuned optical lattice light are shown as *arrows*.

The expression for the well depth V_0 contains the resonant Rabi frequencies Ω_1 and Ω_2. The calculation of these frequencies is complicated by the fact that sodium is by no means a system with a two-level structure, as can be seen in the term diagram for the levels contributing to the sodium D_2 line in Fig. 8.1. However, several factors make a determination of the well depth possible. Our initial condition (before the atoms interact with the light) is such that almost all atoms populate the hyperfine $F = 2$ level in the lower manifold. For linearly polarized light, all of the (nearly) degenerate m_F levels experience the same level shift in the far-detuned regime. Therefore the entire sample experiences the same effective potential [9, 32]. The actual dipole coupling for a particular ground state sublevel $|F\ m_F\rangle$ is obtained by summing over its couplings to all of the available excited states. When the detuning is large compared to the excited state frequency splittings, all of the excited states participate, and the detuning for each excited state is approximately the same. In addition, the dipole coupling summed over all excited states and all polarizations is independent of the m_F sublevel considered [32, 40]. Because of the spherical symmetry of the dipole operator, the three Cartesian components in this sum are equal and therefore the effective dipole coupling for the case of linearly polarized light and large detuning, regardless of the ground state population, is one-third the square of the dipole matrix element for the full D_2 ($J = 1/2 \leftrightarrow J' = 3/2$) transition

$$|d_{\text{effective}}|^2 = \frac{e^2|D_{12}|^2}{3} \ . \tag{8.14}$$

The dipole matrix element $e^2|D_{12}|^2$ can be obtained from the Einstein A coefficient,

$$A_{21} = \Gamma = \frac{1}{\tau} = \frac{\omega_0^3 e^2 |D_{12}|^2}{3\pi\varepsilon_0 \hbar c^3} \frac{2J+1}{2J'+1} , \tag{8.15}$$

which is related to the radiative lifetime [25]. Here, $J = 1/2$ is the ground state and $J' = 3/2$ is the excited state. The radiative lifetime, $\tau = 16.2$ ns, is known empirically. Using Eqs. (8.14) and (8.15), the effective dipole moment is then

$$d_{\text{effective}} = \sqrt{\frac{\varepsilon_0 \hbar \lambda_{\text{L}}^3}{4\pi^2 \tau}} = 1.71 \times 10^{-29} \text{ cm} . \tag{8.16}$$

The time-averaged intensity (defined as the absolute value of the Poynting vector) of a beam of light is related to the amplitude of the electric field by $I = \frac{1}{2} c\varepsilon_0 E^2$. Using this relation together with Eqs. (8.7) and (8.13) yields an expression for the well depth in terms of measurable quantities

$$V_0 = \frac{2\pi c^2}{\tau \omega_0^3} \frac{\sqrt{I_1 I_2}}{\Delta_{\text{L}}} , \tag{8.17}$$

where I_1 and I_2 are the intensities of the traveling wave components.

8.1.4 Spontaneous Emission Rate

In deriving the Hamiltonian for our system, we made the assumption that spontaneous emission can be neglected. Since spontaneous emission is the largest source of decoherence, this statement needs to be quantitatively verified. The total spontaneous photon scattering rate is given by the product of the lifetime and the (steady state) excited state population. Ignoring collisional relaxation we have for the scattering rate [25, 40]

$$R_{\text{sc}} = \left(\frac{\Gamma}{2}\right) \frac{S}{1 + S + 4(\Delta_{\text{L}}/\Gamma)^2} , \tag{8.18}$$

where the *saturation parameter* is given by

$$S = \frac{I}{I_{\text{sat}}} = 2\left(\frac{\Omega}{\Gamma}\right)^2 . \tag{8.19}$$

Using Eq. (8.7) the saturation intensity I_{sat} can be expressed as

$$I_{\text{sat}} = \frac{c\varepsilon_0 \Gamma^2 \hbar^2}{4 d_{\text{effective}}^2} . \tag{8.20}$$

For a linearly polarized far-detuned light beam, we can use the effective dipole matrix element defined in Eq. (8.16) and obtain $I_{\mathrm{sat}} = 9.39\ \mathrm{mW/cm^2}$. For a large detuning we can also approximate the scattering rate as

$$R_{\mathrm{sc}} \approx \frac{\pi \Gamma}{\Delta_{\mathrm{L}}} \frac{V_0}{h} , \tag{8.21}$$

where we have used the definition of the well depth for equal beam intensities as in Eq. (8.13). For typical experimental parameters of $V_0/h = 80$ kHz and $\Delta_{\mathrm{L}} = 2\pi \times 40$ GHz, we get $R_{\mathrm{sc}} = 60\ \mathrm{s}^{-1}$ or roughly one event every 20 ms. For the tunneling experiments of Sect. 8.5, where the requirements on the spontaneous emission were the most stringent, the relevant interaction duration (the time of large acceleration) was at most 100 μs. In this time, less than 1% of the atoms scattered a spontaneous photon.

8.2 Experimental Apparatus

Three important steps were necessary to perform our experiments: the preparation of the initial condition, the generation and application of the interaction potential, and the measurement of the final state of the atoms. To outline the experimental sequence, a simplified schematic is shown in Fig. 8.2. We will give only a brief

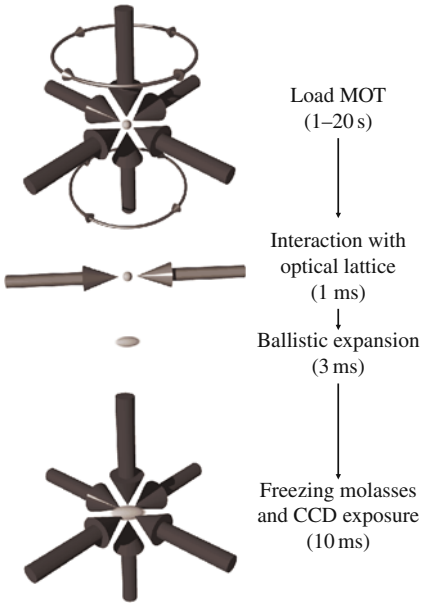

Fig. 8.2 Schematic of the experimental sequence. First the atoms are collected and cooled in a magneto-optic trap. The trapping fields are extinguished and the optical interaction potential is introduced. After interacting with the optical lattice, the atoms are allowed to expand freely in the dark. Finally, the cooling beams are turned on, freezing the atoms in place, and the fluorescence is imaged onto a charge-coupled device (CCD) camera

description of these steps; more details can be found in [11]. The starting point for the interaction was an atomic cloud that was trapped and cooled in a magneto-optic trap (MOT) in the standard $\sigma^+ - \sigma^-$ configuration [6, 37]. Loading sodium atoms from the thermal background into the MOT typically resulted in a cloud of 3×10^5 atoms with a final Gaussian distribution with a width of $\sigma_x = 0.3$ mm in position and $\sigma_p = 6\,\hbar k_\mathrm{L}$ in momentum, where $\hbar k_\mathrm{L}$ is the momentum of a single photon of resonant light. The trapping and cooling fields were then switched off and the interaction beams were turned on. The details of the generation of the interaction potential is given below. After a typical interaction duration of not more than a few milliseconds, the light beams were turned off and the atoms were allowed to expand freely. During this period of ballistic expansion, each atom moved a distance proportional to its velocity. This allowed us to determine the velocity distribution by recording the spatial distribution of the atomic cloud. For this purpose the resonant light was turned on after the free drift period to produce a viscous optical molasses that halted the ballistic motion of the atoms and provided spontaneously scattered resonant light for detection. This light was imaged onto a charge-coupled device camera (CCD) to obtain the desired spatial information. Nonuniform detection efficiencies within the optical molasses were measured and compensated for during data analysis.

8.3 Details of the Interaction

The optical potential was formed by overlapping two linearly polarized traveling waves with parallel polarization vectors. Both beams were derived from the same laser in order to reduce sensitivity to frequency fluctuations originating in the laser. A schematic of the setup is shown in Fig. 8.3. The overall power of the beams was adjusted by an acousto-optic modulator (AOM1). The frequencies of the two beams were controlled independently by two acousto-optic modulators (AOM2 and AOM3). During the tunneling experiments described in Sect. 8.5 the atoms needed to be accelerated to a velocity of up to 3 m/s. This corresponds to $100\,v_\mathrm{r}$, where v_r is the single photon recoil velocity of the atom. To reach this velocity, the counterpropagating beams need to differ in frequency by 10 MHz. During the experiment the frequency difference needed to be adjusted from zero to this maximum value without misalignment. For this reason a double-pass AOM setup was chosen. The frequency of the double-passed beam was scanned, whereas the frequency of the counter-propagating beam was held constant. The beam in the variable frequency arm of the arrangement was focused by a lens through the acousto-optic modulator (AOM3) operating at 40 MHz $\pm\Delta\nu$. An identical lens was placed after the AOM in the first-order diffracted beam. The undeflected portion of the beam was discarded. After being reflected by a mirror the diffracted beam retraced its path through AOM3 and was diffracted again in the same manner. The beam was deflected twice on its path through the AOM, and the frequency was therefore downshifted by twice the drive frequency. Any change in the drive frequency of AOM3 led to an angle change of the first-order diffracted beam, but the beam completing

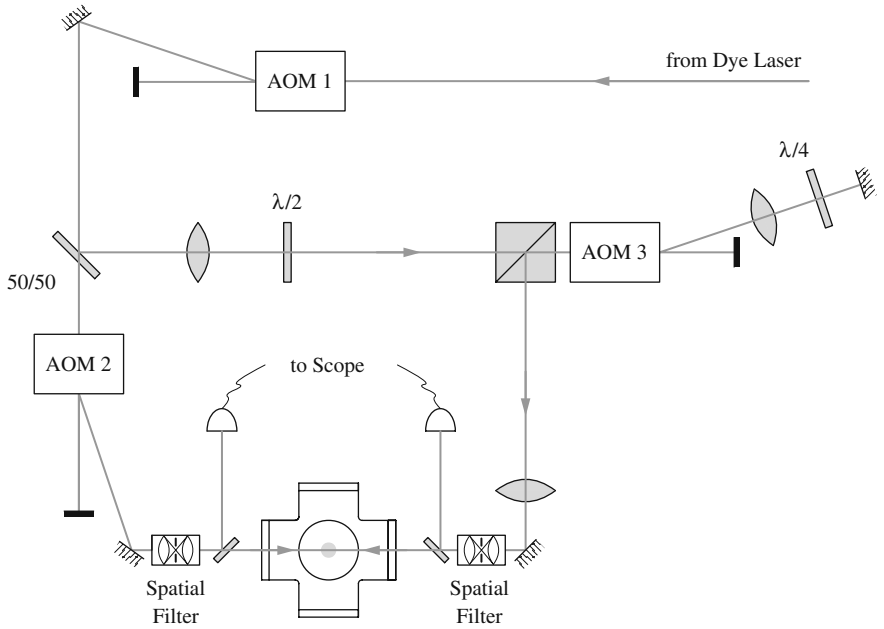

Fig. 8.3 Schematic of the interaction beam setup. AOM1 (40 MHz) provides the global control of the intensity. AOM3 is a double-passed, 40 MHz AOM shifting the beam frequency down by twice its drive frequency without leading to an appreciable angular deflection. AOM2 is in the single-passed configuration shifting down the beam frequency by 80 MHz

both passes through the AOM was still overlapped with the incoming beam regardless of the deflection angle. To separate the backreflected from the incoming beam the polarization was rotated along the path with a quarter-wave plate ($\lambda/4$) so that a polarization beam splitter cube could be used for separation. To compensate for the frequency offset of 80 MHz introduced by AOM3, the frequency in the second arm was down-shifted by AOM2, also by 80 MHz. The frequency difference between both beams was therefore $2\Delta\nu$. After passing through the acousto-optic modulators each beam was spatially filtered. The resulting transverse beam intensity profiles were approximately Gaussian with a beam radius of about 2 mm. The size and divergence of the beams were matched to avoid transverse spatial interference fringes, which could have created local variations of the well depth. A small part of each beam was diverted onto a photodiode to measure the optical power (the calibration accuracy was about 10%).

8.4 Quantum Transport

The system of ultra-cold atoms in a periodic optical potential offers a unique means of studying solid state effects with quantum optics tools. In order to gain insight into the possibilities for experiments, some of the basic properties of this system

will be reviewed. A thorough treatment of the fundamental properties can be found in many solid state textbooks, such as Ashcroft and Mermin [2] or Marder [30]. The specifics of our system are described more thoroughly by Fischer [11].

8.4.1 Stationary Lattice

We created the optical potential by spatially overlapping two counterpropagating light beams ($\mathbf{k_L} \equiv \mathbf{k}_2 = -\mathbf{k}_1$), which yields $\mathbf{q} = \mathbf{k}_2 - \mathbf{k}_1 = 2\mathbf{k_L}$. Choosing the same frequency for both beams simplifies the effective Hamiltonian in Eq. (8.12) to

$$H = \frac{p^2}{2M} + V_0 \cos(2k_L x) \ , \tag{8.22}$$

assuming that beam propagation is along the x-axis. This form of the Hamiltonian is a textbook example for a particle placed in a spatially periodic potential, and many general properties of this system can be derived by symmetry arguments alone. The most fundamental properties are expressed in *Bloch's theorem*. It states that the eigenstates $\psi(x)$ of this Hamiltonian take on the form of a plane wave multiplied by a function $u(x)$ of periodicity $d = \frac{\pi}{k_L} = \frac{\lambda}{2}$ (the periodicity of the potential):

$$\psi_{n,k}(x) = e^{ikx} u_{n,k}(x) \ , \tag{8.23}$$

where k is the quasi-momentum of the particle. The index n is called the *band index* and appears in Bloch's theorem because for a given k there are many solutions to the Schrödinger equation. An important consequence of Bloch's theorem is that the wave functions and the energy dispersion of the particle are periodic in quasi-momentum (reciprocal) space with a periodicity of $K = \frac{2\pi}{d} = 2k_L$ in reciprocal space. Another property of paramount importance concerns the mean velocity of a particle in a particular Bloch state $\psi_{n,k}$. It can be shown that the velocity is determined by the energy dispersion relation as

$$v_n(k) = \frac{1}{\hbar} \frac{\partial E_n(k)}{\partial k} \ , \tag{8.24}$$

in analogy to the free particle case [2].

The problem of finding the energy eigenstates of H, that is solving $H|\psi\rangle = E|\psi\rangle$, is equivalent to solving Mathieu's equation [1]. Sample dispersion curves (energy versus the quasi-momentum k) were calculated and plotted in Fig. 8.4. For a vanishing well depth V_0 the dispersion curve is the free particle energy parabola $E(k) = \frac{\hbar^2 k^2}{2M}$. For a finite well depth V_0, the lowest crossing points of the free energy parabolas at $k = \pm k_L$ develop a level repulsion due to the coupling of the levels by the potential term. The amount of repulsion in this *avoided level crossing* can easily

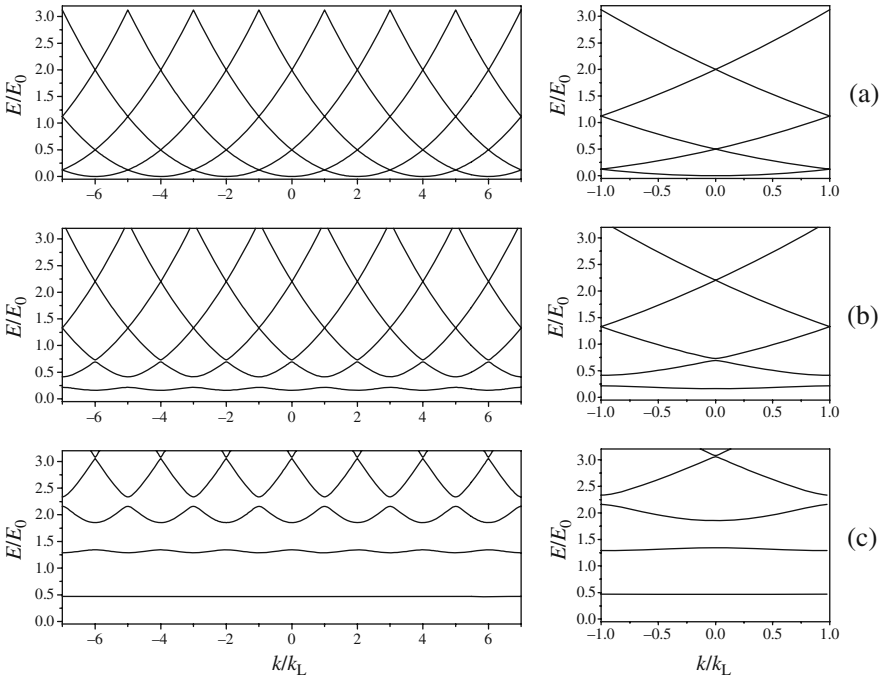

Fig. 8.4 Dispersion curves of a particle in a sinusoidal potential. Plotted here are the energy (in units of $E_0 = 8\,\hbar\omega_r$, $\hbar\omega_r$ being the recoil energy) versus the quasi-momentum k (in units of k_L) in the repeated-zone scheme (*left panels*) and in the reduced-zone scheme (*right panels*). The well depth V_0/h of the potential is (**a**) 0, (**b**) 40 kHz, and (**c**) 200 kHz

be estimated by first-order degenerate perturbation theory. The eigenenergies of the coupled system are

$$E_{1,2} = \frac{\hbar^2 k_L^2}{2M} \pm \frac{1}{2} V_0 \,. \tag{8.25}$$

The energy splitting for the first crossing and therefore the width of the first band gap is, to first order in V_0, equal to V_0 itself. The coupling term $\cos(2k_L x)$ connects only states with a difference in momentum of $2\,\hbar k_L$. For the calculation of the splitting at higher crossing points, we therefore need to resort to perturbation expansions of higher order.

The energy values evaluated at the band edges as a function of the well depth V_0 have been determined numerically and are displayed in Fig. 8.5. From this figure one can see that the energy bands evolve from a continuum of allowed energies, for a vanishing well depth, into the linearly spaced discrete energy levels of a harmonic oscillator, in the limit of large well depth.

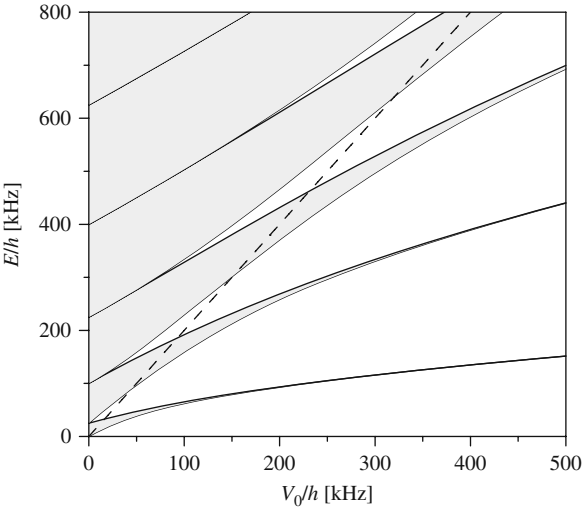

Fig. 8.5 Regions of allowed (*gray*) and restricted (*white*) energy in the periodic potential as a function of the well depth. The energy is measured relative to the bottom of the well. Indicated as a *dashed line* is the top edge of the potential ($2V_0$)

8.4.2 Accelerating Lattice

For the system of electrons in a crystal lattice, the most commonly encountered perturbation is an applied static electric field. This seemingly simple perturbation leads to a very rich system, whose properties were controversial for quite some time. Experimental tests in the field of solid state physics were hindered by decohering processes such as scattering of the electrons on impurities in the crystal lattice or scattering among themselves. These effects are negligible in our atom optics system and we were able to contribute to this field by studying some of the effects previously inaccessible to experiment.

8.4.2.1 Semiclassical Equations of Motion

A static electric field, which exerts a strong force on the electrons in a crystal, does not have the desired effect on a neutral atom in an optical potential. However, we can simulate the corresponding force by introducing an appropriate time dependence of the optical lattice. Let us consider an optical lattice composed of two counterpropagating light beams of unequal frequencies. A constant acceleration of the "standing" wave pattern is generated by linearly chirping the frequency difference of these counterpropagating beams. This is described by $\phi(t) = k_{\mathrm{L}} a t^2$ in Eq. (8.12), where a is the acceleration. Inserting this into the Hamiltonian yields

$$H = \frac{p^2}{2M} + V_0 \cos\left[2k_{\mathrm{L}}\left(x - \frac{1}{2}at^2\right)\right] . \tag{8.26}$$

To make the connection to the solid state system, one can transform Eq. (8.26) to the frame of reference accelerated with the potential by applying a unitary transformation, following Peik et al. [36], resulting in

$$\tilde{H} = \frac{p^2}{2M} + V_0 \cos(2k_{\mathrm{L}} x) + Ma\, x \ . \tag{8.27}$$

The last term containing the mass M of the atom is an inertial term, resulting from the transformation to an accelerating frame of reference. It mimics the role of the interaction potential $U_{el} = \mathcal{E} e\, x$ between an electric field $\mathcal{E}$ and the electron of charge e. Having established this connection, we can directly apply the results for the solid state system to an atom in the accelerated optical potential. A derivation of the semiclassical equations of motion for small electric fields can be found in standard textbooks [2, 30] and are simply stated here without proof. They express the relationship of the state's quasi-momentum k, band index n, energy $E_n(k)$, and mean velocity $v_n(k)$. By replacing the force $F = e\,\mathcal{E}$ with $F = Ma$, we obtain the following statements:

1. The band index n is a constant of motion.
2. The expression for the velocity in Eq. (8.24) remains unchanged and the evolution of the quasi-momentum is described by

$$\dot{k}_n(t) = -\frac{1}{\hbar} Ma \ . \tag{8.28}$$

3. The form of the band structure $E_n(k)$ is unchanged.

The restriction of *small fields* deserves special attention. The statement that the band index is a constant of motion indicates that inter-band transitions are being neglected. However, for larger fields electrons can tunnel across the band gap. An estimate for a "small" field strength is given by Ashcroft and Mermin as $E \ll \frac{E_{\mathrm{g}}^2}{e\hbar v_{\mathrm{F}}}$, with v_{F} being the typical electron velocity in the originating band and E_{g} being the minimum energy separation of the perturbed levels [2]. In our system this transforms to a condition for the acceleration

$$a \ll \frac{E_{\mathrm{g}}^2}{\hbar^2 k_{\mathrm{L}}} \ , \tag{8.29}$$

where $v_{\mathrm{r}} = \hbar k_{\mathrm{L}}/M$ serves as the typical velocity at the edge of the Brillouin zone. Since for higher band indices the gaps get smaller and the velocity gets higher, a dramatic increase in the tunneling probability is to be expected. A more detailed study of tunneling across band gaps will be provided in Sect. 8.5.

8.4.2.2 Bloch Oscillations and Wannier–Stark States

One remarkable consequence of the equations of motion stated above is that particles exposed to a static field are predicted to oscillate in space rather than increase their velocity steadily. As can be seen by integrating Eq. (8.28), the quasi-momentum increases linearly with time as

$$k(t) = k_0 - \frac{Mat}{\hbar} \,. \tag{8.30}$$

The velocity of the particle with a given quasi-momentum k is given by Eq. (8.24) as the derivative of the dispersion curve at the point k. Since $E_n(k)$ is oscillatory in reciprocal space and k varies linearly with time, the velocity $v_n(t)$ is oscillatory in time. The period of oscillation τ_B is the time it takes for a particle to traverse the Brillouin zone of width $K = 2k_\mathrm{L}$ and calculates to

$$\tau_\mathrm{B} = \frac{2\hbar k_\mathrm{L}}{Ma} = \frac{2v_\mathrm{r}}{a} \,. \tag{8.31}$$

A sketch of these *Bloch oscillations* is graphically depicted in Fig. 8.6(a). An atom starting in the lowest band of the potential will increase its quasi-momentum k due to the applied force, as given by Eq. (8.30). As it approaches the edge of the Brillouin zone at a constant rate $\partial_t k$, the velocity decreases as the slope of the dispersion curve decreases. At $k = k_\mathrm{L}$ the derivative $\partial_k E_0(k)$ is zero and according to Eq. (8.24) the particle is at rest. It will then reverse its velocity and continue its motion, until the velocity is reversed again at the next minimum of the dispersion curve. The reversal of its velocity at $k = k_\mathrm{L}$ can be viewed as a first-order Bragg reflection of the particle wave by the periodic potential. The arguments above also hold for atoms in higher bands. They oscillate at the same Bloch frequency. However, the velocity reversal in higher bands corresponds to a higher order Bragg scattering process. It is important to note that this reversal of the atomic velocity occurs relative to the accelerated frame. In the laboratory frame the constant acceleration of the potential is superimposed on the oscillation of the atom.

For a higher field strength (or acceleration, in the atom optics system) the particle might not be able to follow the dispersion curve adiabatically as it approaches the edge of the Brillouin zone. It can cross the band gap and continue its motion in a higher band, as indicated in Fig. 8.6(b). This corresponds to a tunneling process through the band gap, in which case the semiclassical equations stated above no longer hold. For a particle undergoing tunneling, the transformation back to the laboratory frame reveals no change of velocity at all. The particle is simply lost out of the potential and can no longer track the acceleration.

The Bloch bands of an atom in a stationary potential are, by definition, continuous regions in the energy spectrum. Bloch oscillations in an accelerated lattice reveal themselves in the energy spectrum as discrete peaks with an energy separation of $h\nu_\mathrm{B}$, where $\nu_\mathrm{B} = 1/\tau_\mathrm{B}$. This is a consequence of the Bloch bands splitting up into discrete *Wannier–Stark states*. A physical interpretation of these states can be

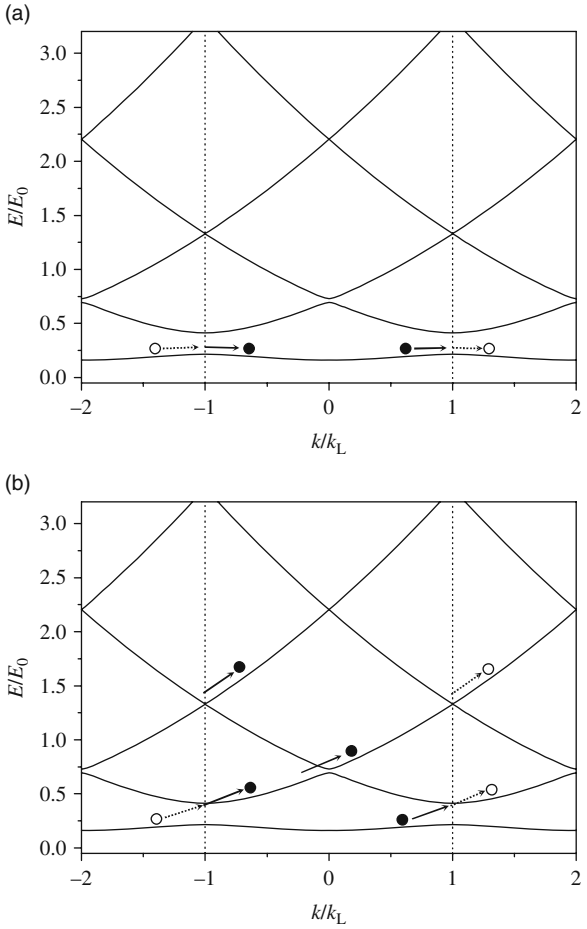

Fig. 8.6 Sketch of a particle trajectory in reciprocal space. In the *upper panel* (**a**) the rate of change of the quasi-momentum is slow enough for the particle to follow the dispersion curve adiabatically across the Brillouin zone boundary. This is equivalent to discontinuing the motion at one edge of the Brillouin zone and emerging from the other side in the same band. The *lower panel* (**b**) illustrates a case for a larger force, where the particle cannot follow the curve and tunnels through the band gap

obtained by regarding the transition between bands as a temporal interference effect. Quantum mechanically, atoms can tunnel between bands at all positions within the Brillouin zone. Since Bloch oscillations lead to multiple passes through the Brillouin zone, transition amplitudes can interfere constructively or destructively, depending on the rate at which the particle traverses the Brillouin zone. This is in analogy to the optical interference pattern generated by a plane wave of light illuminating an array of slits or a grating. The temporal interference produces sharp resonances spaced at the (temporal) grating period τ_B. The more traversals of the Brillouin zone the

particle completes, the sharper the resonance becomes. If the particle tunnels out of the band quickly, the resonances are broad, indicating a short lifetime of the associated state. The tunneling out of a bound state is enhanced by the presence of a Wannier–Stark state of the same energy, but in a higher band and displaced by one or more lattice sites. This situation is depicted in Fig. 8.7(a).

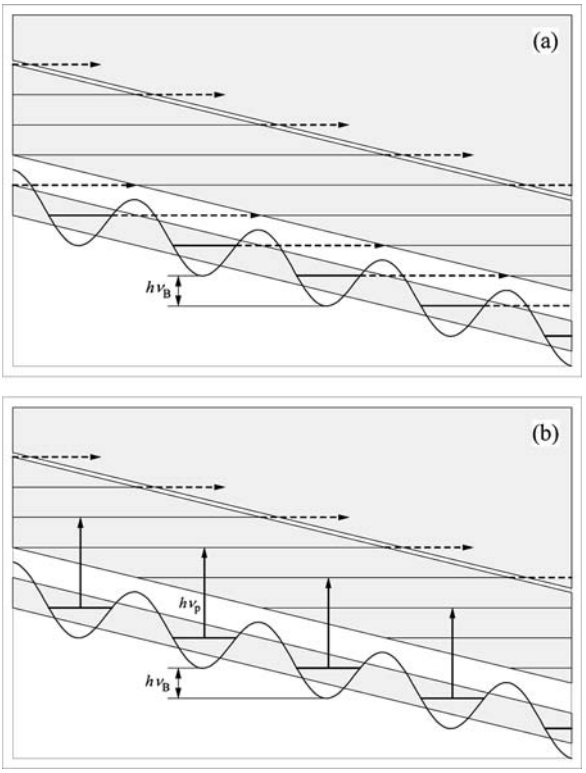

Fig. 8.7 Schematic of the Wannier–Stark ladder within the bands. In (**a**) the tunneling process is indicated. The presence of a Wannier–Stark state in the continuum of the higher band enhances the tunneling probability across the gap. In (**b**) a weak spectroscopic drive couples the states and introduces transitions. In either case, once an atom is in the second band, it can easily tunnel across successive band gaps into higher bands

Krieger and Iafrate [23] also consider the possibility of driving transitions between bands with an external alternating probe field. Assuming that the transition due to the probe drive is the dominant loss process from the first band (neglecting tunneling), they obtain a resonance condition for the drive frequency ν_p

$$\nu_p = \frac{\bar{E}_g}{h} + n\nu_B \ , \tag{8.32}$$

where $\bar{E}_g$ is the average band separation. Here, the driving field provides a direct spectroscopic tool to probe the lattice structure of the Wannier–Stark states by allowing transitions between the states, as indicated in Fig. 8.7(b).

8.4.3 Band Spectroscopy and Wannier–Stark Ladders

In our experiments the initial atomic distribution was approximately Gaussian with a width of $\sigma_x = 0.3$ mm in position and $\sigma_p = 6\,\hbar k_L$ in momentum. However, to be able to study tunneling and transitions between single bands, an initial condition with only one populated band, preferably the lowest, was desired. If we suddenly turn on the optical potential within the atomic distribution, only a fraction of the atoms are transferred into the lowest band [35]. Most atoms will be projected into higher index bands. The location of the bands relative to the potential is indicated in Fig. 8.5. For a typical well depth of $V_0/h = 70$ kHz, we can see that atoms in the lowest band are trapped within the potential wells, whereas atoms in the second band are only partially trapped. Atoms in even higher bands have energies well above the potential and hence are effectively free. The location of the bands with respect to the potential well can be regarded as an indicator for the tunneling rates between bands when an acceleration is applied. Bands that lie entirely within the wells have a much smaller tunneling rate than bands outside the range of the potential. To empty all but the lowest band, we took advantage of this difference in tunneling rates across successive band gaps. After turning on the standing wave, it was accelerated to a velocity of $v_0 = 40\,v_r$, as indicated in Fig. 8.8. During this acceleration the atoms in the first band performed a sequence of Bloch oscillations within the potential and were accelerated in the laboratory frame. Atoms in higher bands could tunnel through the successively smaller band gaps and were lost out of the potential. The transport acceleration a_{trans} was chosen to maximize tunneling out of the second band while minimizing losses from the first trapped band. For typical experimental parameters of $V_0/h = 70$ kHz and $a_{trans} = 2000$ m/s^2, the Landau–Zener expression derived in Sect. 8.5 for the lifetime of the first and second band yields 24 ms and 40 μs, respectively. This ensured that after 600 μs of acceleration only the first band still contained a significant number of atoms.

For band spectroscopy experiments the frequency chirp was stopped after reaching the velocity v_0 and the frequency difference was held constant. At that point, a phase modulation at the frequency of ν_p was added to one of the two counter-propagating beams forming the standing wave, as indicated in Fig. 8.8. This phase modulation could drive transitions between bands, if the band separation for some value of k was close to $E = h\nu_p$. The modulation typically lasted for 500 μs and was switched on and off smoothly over 16 μs to avoid any discontinuous phase changes in the potential that could induce transition to higher bands. The amplitude of the modulation was chosen to be small enough to not perturb the band structure.

In order to study Wannier–Stark states experimentally a constant acceleration of the optical potential was necessary. Therefore the frequency chirp was not stopped

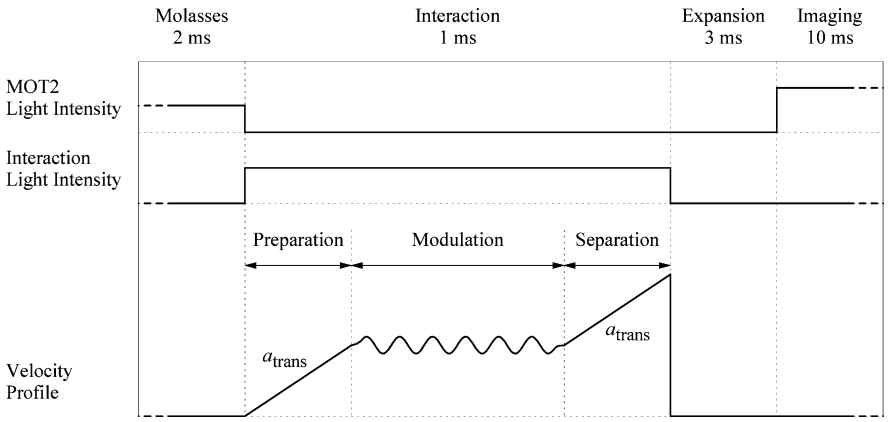

Fig. 8.8 Interaction beam timing diagram for the band spectroscopy experiments. After the molasses stage the resonant light is turned off and the optical lattice was turned on. A subset of atoms is projected into the fundamental band and separated in velocity by an acceleration a_{trans}. After this preparation stage, the optical lattice position and amplitude are varied to realize the potential under study. This step is followed by separating the atoms in the lowest band from those in higher bands by the same acceleration a_{trans}. The atoms are then allowed to expand freely in the dark and the spatial distribution is illuminated with the resonant molasses light

during the modulation time but was adjusted to yield the desired value of the acceleration a. To spectroscopically investigate the states, we superimposed the phase modulation at frequency ν_{p} onto this frequency chirp.

After a fixed time interval the modulation was turned off and the frequency chirping resumed at a rate corresponding to a_{trans}. This separated in momentum space the remaining trapped atoms in the lowest band from those having made the transition into higher bands. After reaching a final velocity $v_{\text{final}} = 80\, v_{\text{r}}$, the interaction beams were switched off suddenly.

In the detection phase we needed to distinguish three classes of atoms: (1) atoms that were not initially trapped in the lowest band and immediately tunneled out of the well during the initial acceleration, (2) atoms which were trapped in the first band at the beginning of the interaction but were driven out by the modulation, and (3) atoms that remained in the first band during the entire sequence. Since the atoms in different classes had left the trapping potential at different stages of the experimental sequence, they were accelerated to different velocities. Therefore, after drifting in the dark for 3 ms, these classes separated in space and could be distinguished by recording their position. For this purpose the atoms were imaged in the "freezing molasses" as described in Sect. 8.2. A typical fluorescence image of the atoms is shown in Fig. 8.9(a). The two-dimensional image was then integrated in the direction perpendicular to the axis of the interaction beams to obtain a one-dimensional distribution along the beam direction, containing all three classes of atoms. The corresponding integrated distribution is shown in Fig. 8.9(b). In order to reduce sensitivity to fluctuations of the number of atoms in the MOT, the number of survivors (atoms in class (3)) was normalized by the total number of atoms initially

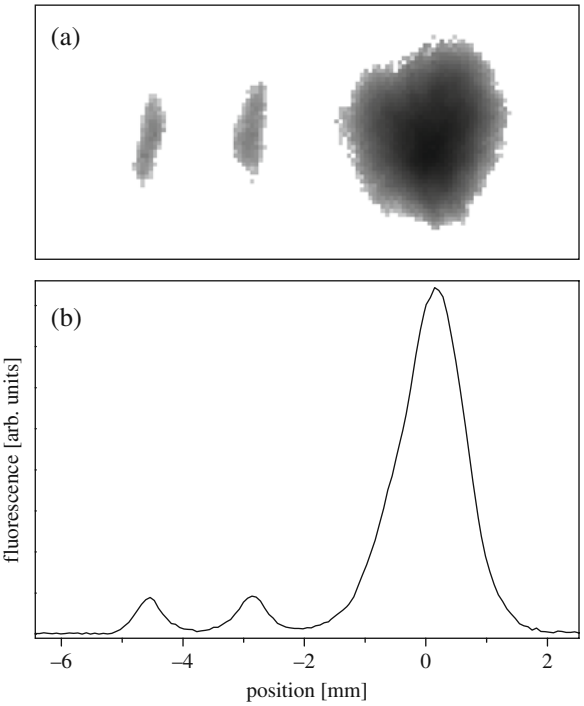

Fig. 8.9 Part (**a**) shows a fluorescence image from an atomic distribution acquired after a time of ballistic expansion. Part (**b**) shows the distribution integrated in the vertical direction. The large peak on the *right* is the part of the atomic cloud that was not trapped during the initial acceleration. The *center* peak indicates the atoms that were initially trapped in the first band but were driven out by the modulation. The *left* peak corresponds to atoms that remained trapped during the entire sequence. The survival probability is the area under the *left* peak normalized by the sum of the areas under the *left* and *center* peak

trapped in the first band, which was obtained by summing the contributions of class (2) and class (3).

To observe the temporal evolution of the fundamental band population, we repeated the sequence in Fig. 8.8 for various modulation durations, holding the probe frequency ν_p and amplitude m fixed. These studies resulted in the observation of Rabi oscillations between Bloch bands [13]. For large amplitudes of the modulation, we observed a *dynamical suppression* of the band structure, effectively turning off Bloch tunneling [28].

To obtain a spectrum of the Wannier–Stark states, we applied the modulation during a period of constant acceleration and repeated the sequence for various probe modulation frequencies, holding the modulation amplitude m and the duration fixed. Figure 8.10 shows three measured spectra for the accelerations of 947, 1260, and 1680 m/s^2, which correspond to the Bloch frequencies $\omega_B/2\pi = 16.0$, 21.4, and 28.5 kHz, respectively. The spectra were obtained at a fixed well depth of $V_0/h = 91.6$ kHz and a fixed probe modulation amplitude of $m = 0.05$. For a well depth

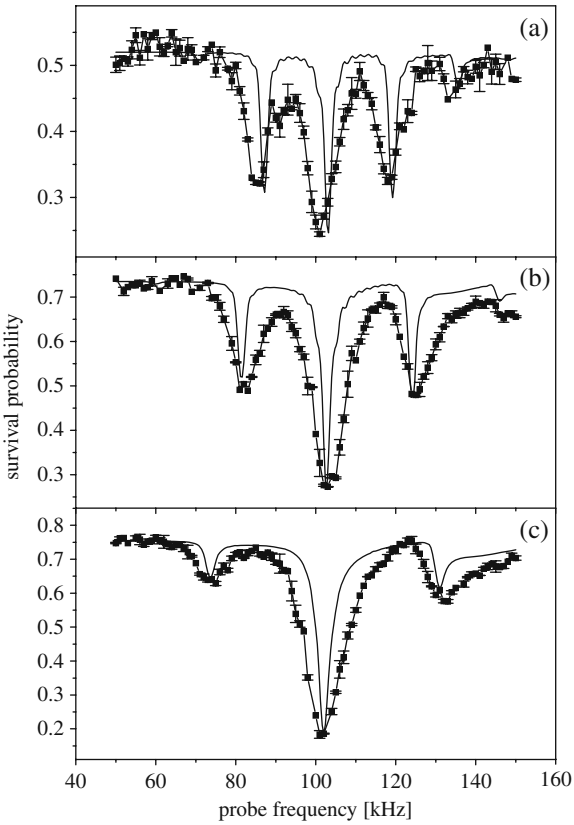

Fig. 8.10 Wannier–Stark ladder resonances for a well depth of $V_0/h = 91.6$ kHz and accelerations of (**a**) 947 m/s^2, (**b**) 1260 m/s^2, and (**c**) 1680 m/s^2, which correspond to the Bloch frequencies $\omega_B/2\pi = 16.0$, 21.4, and 28.5 kHz, respectively. For the chosen well depth, the average band spacing is $\bar{E}_g/h = 104$ kHz which is in good agreement with the location of the central resonance. The points are connected by *thin solid lines* for clarity. The *thick solid lines* show the results of numerical simulations using the experimental parameters. Figure from [29]; Copyright 1999 by the American Physical Society

of $V_0/h = 91.6$ kHz, the average band spacing is $\bar{E}_g/h = 104$ kHz, which is in good agreement with the location of the central resonance in the three spectra of Fig. 8.10.

Also shown in Fig. 8.10 is the result of a numerical integration of the time-dependent Schrödinger equation using the experimental parameters. We believe that phase noise in the interaction beams prevented the survival probability from reaching unity, when the probe was far from resonance, and reduced the depth of the spectral features by a constant factor. For this reason, the y-values of the theory curves were shifted and scaled to match the baseline and amplitude of the central resonance. In addition, the value for the probe modulation amplitude m was

adjusted in the numerical simulations from 0.05 to 0.035 to reproduce the relative peak heights.

The spectral width of the resonances is fundamentally determined by the finite lifetime of the Wannier–Stark states due to tunneling. However, a number of experimental mechanisms (e.g., phase noise in the standing wave beams, variations in the well depth, or the finite transverse extent of the optical potential) contributed to the measured width being substantially broader than that predicted by the simulations.

8.5 Quantum Tunneling

In the previous section we studied the spectral features of Bloch states and Wannier–Stark states by driving transitions between those states. These inter-band transitions were imposed externally by a modulation of the potential. Without modulation the band index was conserved. The accelerations that transported the atoms through reciprocal space were small enough to preserve the validity of the semiclassical equations of motion. In this section we investigate the effect of a large acceleration of the optical potential. In this case the semiclassical equations no longer hold and inter-band tunneling can occur. The atoms can leave the trapping potential via tunneling into the continuum of free states. The system is therefore unstable and the number of trapped atoms decays with time. By adjusting the acceleration the stability of the system can be altered dynamically and the decay rates vary over a wide range. In this system, short-time deviations from the universal exponential decay law are observed [42]. In addition, we study the fundamental effects of measurements on the decay rate and report on the first observation of the quantum Zeno and anti-Zeno effects in an unstable system [12].

8.5.1 Classical Limit

As derived in Sect. 8.4, atoms in an accelerated standing wave are subject to a potential

$$V(x) = V_0 \cos(2k_L x) + Max \ . \tag{8.33}$$

This potential is stated in the reference frame accelerated with the potential as given in Eq. (8.27). For a small enough acceleration a particle can be classically trapped within the wells of this "washboard" potential. In this case the particle will accelerate along with the potential. For a larger acceleration the potential wells become increasingly asymmetric up to a point where the particle is no longer confined by the potential. The critical acceleration $a_{c,class}$, for which the potential loses its ability to confine the particle, can be found by solving for extrema of the potential in Eq. (8.33), which only exists for

$$|a| < a_{c,class} = \frac{2k_L V_0}{M} \ . \tag{8.34}$$

For accelerations smaller than $a_{\mathrm{c,class}}$ the particle gets accelerated along with the potential whereas for larger accelerations there are no local potential minima.

8.5.2 Landau–Zener Tunneling

8.5.2.1 Tunneling Rates

In this section we provide a short description of the Landau–Zener tunneling process based on diabatic transitions in momentum space [35, 44]. An alternative description can be derived in the position representation [26, 45]. As a starting point we consider the semiclassical equations of motion describing the time evolution of the quasi-momentum in reciprocal space. In order to allow for inter-band transitions, we must now abandon the condition that the band index be a constant of motion. The shape of the Bloch bands and the time evolution equation for the quasi-momentum are still assumed to be valid. The stationary periodic potential causes the free particle energy levels to undergo a level repulsion. This shift is most pronounced at the edges of the Brillouin zone. A particle approaching the avoided level crossing might not be able to follow the dispersion curve adiabatically, in which case it continues its motion and diabatically changes levels across the energy gap. In 1932 Zener derived an expression for the probability P of diabatic transfer between two repelled levels [44]

$$P = \exp\left(-\frac{\pi}{2\hbar}\,\frac{E_{\mathrm{g}}^2}{\frac{\mathrm{d}}{\mathrm{d}t}(\varepsilon_1 - \varepsilon_2)}\right)\,, \tag{8.35}$$

where E_{g} is the minimum energy separation of the perturbed levels and $\varepsilon_{1,2}$ are the unperturbed energy eigenvalues of level 1 and 2, respectively. In our case the unperturbed energy curve is simply the free particle kinetic energy dispersion $E_p = p^2/2M$. Using the semiclassical equation of motion for the quasi-momentum, we obtain for the probability of transfer

$$P = e^{-a_{\mathrm{c}}/a}\,, \tag{8.36}$$

where the critical acceleration a_{c} is given by

$$a_{\mathrm{c}} = \frac{\pi}{4}\,\frac{E_{\mathrm{g}}^2}{n\,\hbar^2 k_{\mathrm{L}}}\,. \tag{8.37}$$

We let N denote the number of particles populating the lowest band within the first Brillouin zone. The rate of atoms crossing the band gap is equal to the rate of atoms approaching the transition region times the probability of tunneling if we assume the band to be uniformly populated. We obtain an exponential decay of the population N in the band under consideration as

$$N = N_0\, e^{-\Gamma_{\mathrm{LZ}}\, t}, \tag{8.38}$$

with the Landau–Zener (LZ) decay rate Γ_{LZ} given by

$$\Gamma_{\mathrm{LZ}} = \frac{a}{2v_{\mathrm{r}}}\, e^{-a_{\mathrm{c}}/a} \ . \tag{8.39}$$

Experimental studies of the tunneling rates out of the lowest band were performed in our group and the decay rates were compared to the Landau–Zener prediction [3, 27].

8.5.2.2 Deviations from Landau–Zener Tunneling

The expression for the LZ tunneling rate derived above is based on a single transit of the atom through the region of an avoided crossing. However, for small tunneling probability the atom can undergo Bloch oscillations within a given band, leading to multiple passes through the Brillouin zone. The tunneling amplitudes can interfere constructively or destructively depending on the rate at which the atom traverses the Brillouin zone. This mechanism is responsible for the formation of tunneling resonances. For small accelerations the tunneling rate is small and the atoms can perform many Bloch oscillations before leaving the band. Therefore large deviations from the Landau–Zener prediction for the tunneling rate are to be expected. For a larger acceleration the atom leaves the band quickly and the interference effects are less pronounced. For those cases the LZ prediction is a good approximation for the actual tunneling rate. These statements are in agreement with the observed tunneling rates [3, 27].

8.5.3 Non-exponential Decay

8.5.3.1 Theoretical Description

An exponential decay law is the universal hallmark of unstable systems and is observed in all fields of science. This law is not, however, fully consistent with quantum mechanics and deviations from exponential decay have been predicted for short as well as long times [20, 43, 14]. In 1957 Khalfin showed that if H has a spectrum bounded from below, the survival probability is not a pure exponential but rather of the form

$$\lim_{t\to\infty} P(t) \approx \exp(-ct^q) \qquad q < 1, c > 0 \ . \tag{8.40}$$

Later Winter examined the time evolution in a simple barrier-penetration problem [43]. He showed that the survival probability begins with a non-exponential, oscillatory behavior. Only after this initial time does the system start to evolve according to the usual exponential decay of an unstable system. Finally, at very long times, it decays like an inverse power of the time. The initial non-exponential decay behavior is related to the fact that the coupling between the decaying system and the

reservoir is reversible for short enough times. Moreover, for these short times, the decayed and undecayed states are not yet resolvable, even in principle.

A simple argument will illustrate this point. We assume that the system is initially in the undecayed state $|\Psi_0\rangle$ at $t = 0$, and that the state evolves under the action of the Hamiltonian H,

$$|\Psi(t)\rangle = e^{-iHt/\hbar}|\Psi_0\rangle = A(t)|\Psi_0\rangle + |\Phi(t)\rangle \,, \tag{8.41}$$

where $A(t)$ is the probability amplitude for remaining in the undecayed state and the state $|\Phi(t)\rangle$ denotes the decayed state with $\langle\Psi_0|\Phi(t)\rangle = 0$. The probability of survival P in the undecayed state is therefore $P(t) = |A(t)|^2$. Acting with the time evolution operator $e^{-iH(t+t')/\hbar}$ on the state $|\Psi_0\rangle$ yields

$$A(t+t') = A(t)A(t') + \langle\Psi_0|e^{-iHt'/\hbar}|\Phi(t)\rangle \,. \tag{8.42}$$

If it were not for the last term, the equation above would generate the characteristic exponential decay law of an unstable system. However, the term under consideration describes the possibility for the decayed state $|\Phi(t)\rangle$ to re-form the initial state $|\Psi_0\rangle$ under the time evolution operator for time t'.

For very short times we can make a general prediction about the time evolution of the survival probability P. Given that the mean energy of the decaying state is finite and that H has a spectrum that is bounded from below, one can show following the arguments of Fonda et al. [14] that

$$\left.\frac{\mathrm{d}P(t)}{\mathrm{d}t}\right|_{t\to 0} = 0 \,. \tag{8.43}$$

As outlined by Grotz and Klapdor [18] we can expand $A(t)$ in a power series

$$A(t) = 1 - i\frac{t}{\hbar}\langle\Psi_0|H|\Psi_0\rangle - \frac{t^2}{2\hbar^2}\langle\Psi_0|H^2|\Psi_0\rangle + O(t^3) \,. \tag{8.44}$$

Using this expansion results in an expression for the survival probability

$$P(t) = |A(t)|^2 = 1 - \frac{t^2}{\hbar^2}\langle\Psi_0|(H-\bar{E})^2|\Psi_0\rangle + O(t^4) \,, \tag{8.45}$$

where $\bar{E} = \langle\Psi_0|H|\Psi_0\rangle$. This form indicates a population transfer beginning with a flat slope and suggests an initial quadratic time dependence.

The results stated here are general properties independent of the details of the interaction. However, the timescale over which the deviation from exponential behavior is apparent depends on the particular timescales of the decaying system. Greenland and Lane point out a number of timescales which are relevant [17]. The first timescale τ_e is given by the time that it takes the decay products to leave the bound state region. This time can be estimated as

$$\tau_e = \frac{\hbar}{E_0} , \tag{8.46}$$

where E_0 is the energy released during the decay. It determines the amount of time required to pass before the decayed and undecayed states can be resolved. The second timescale τ_w is related to the bandwidth ΔE of the continuum to which the state is coupled

$$\tau_w = \frac{\hbar}{\Delta E} . \tag{8.47}$$

The phases of all states in the continuum evolve at a rate corresponding to their energy. Thus after the time τ_w the phases of these states have spread over such a wide range as to prevent the reformation of the initial undecayed state. After this dephasing time, the coupling is essentially irreversible.

Although these predictions are of general nature and applicable in every unstable system, deviations from exponential decay have not been observed experimentally in any other system than the one described here [42]. The primary reason is that these characteristic timescales in most naturally occurring systems are extremely short. For the decay of a spontaneous photon, the time τ_e it takes a photon to traverse the bound state size is approximately an optical period, 10^{-15} s. For a nuclear decay this timescale is orders of magnitude shorter, about 10^{-21} s. By contrast, the dynamical timescale for an atom bound in an optical lattice is just the inverse band gap energy, which in our experiments is on the order of several microseconds.

Niu and Raizen [34] performed a more detailed investigation of a two-band model of our system. They find an initial non-exponential regime that starts with a quadratic time dependence, then becomes a damped oscillation, and finally settles into an exponential decay. The timescale for which the coherent oscillations damp out and the exponential decay behavior sets in is identified as the crossover time t_c equal to

$$t_c = \frac{E_g}{a} \frac{1}{2\hbar k_L} . \tag{8.48}$$

For a typical value for the acceleration of $a = 10,000\ \mathrm{m/s^2}$ and a band gap of $E_g/h = 80$ kHz, the crossover time calculates to $t_c = 2\ \mu$s.

8.5.3.2 Experimental Realization

The preparation of the initial state was done as described previously. After turning on the interaction beams, a small acceleration of $a_{trans} = 2000\ \mathrm{m/s^2}$ was imposed to separate those atoms projected into the lowest band from the rest of the distribution. After reaching the velocity $v_0 = 35\, v_r$, the acceleration was suddenly increased to a value a_{tunnel} where appreciable tunneling out of the first band occurred. Unlike in the band spectroscopy experiments no phase modulation was added to induce

transitions between the bands. The large acceleration a_{tunnel} was maintained for a period of time t_{tunnel}, after which time the frequency chirping continued again at the decreased rate corresponding to a_{trans}. This separated in momentum space the atoms that were still trapped in the lowest band from those in higher bands. After reaching a final velocity of $v_{\text{final}} = 80\, v_{\text{r}}$, the interaction beams were switched off suddenly. A diagram of the velocity profile versus time is shown in Fig. 8.11(a).

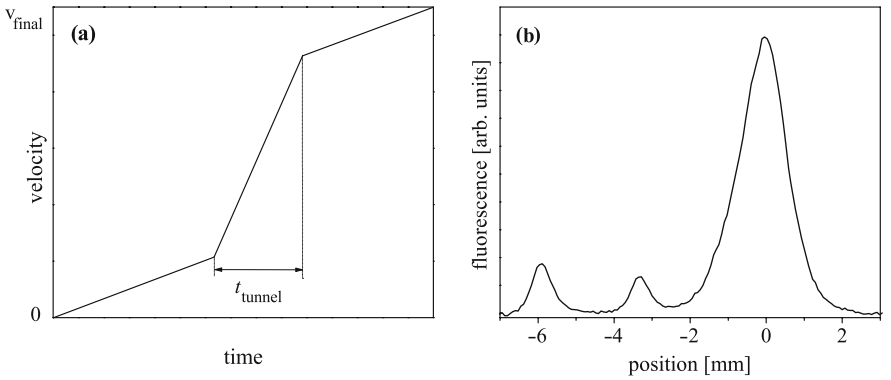

Fig. 8.11 Part (**a**) shows a diagram of the acceleration sequence to study tunneling out of the lowest band. Part (**b**) shows a typical integrated spatial distribution of atoms after ballistic expansion. The large peak on the *right* is the part of the atomic cloud that was not trapped during the initial acceleration. The *center* peak indicates the atoms that tunneled out of the potential during the fast acceleration period. The *leftmost* peak corresponds to atoms that remained trapped during the entire sequence. Figure from [12]; Copyright 2001 by the American Physical Society

In the detection phase we determined the number of atoms that were initially trapped and what fraction remained in the first band after the tunneling sequence. After an atom tunneled out of the potential during the sequence, it would maintain the velocity that it had at the moment of tunneling. During the period of free ballistic expansion the difference in final velocity between trapped and tunneled atoms led to their spatial separation (Fig. 8.11(b)). To observe the temporal evolution of the fundamental band population, we repeated a sequence such as in Fig. 8.11(a) for various tunneling durations t_{tunnel}, holding the other parameters of the sequence fixed.

Figure 8.12 shows the probability of survival in the accelerated potential as a function of the duration of tunneling for various values of the tunneling acceleration a_{tunnel} between 6000 and 20,000 m/s^2. The value for the well depth for all curves was $V_0/h = 92$ kHz. Initially, the survival probability shows a flat region, owing to the reversibility of the decay process for short times. At intermediate times the decay shows a damped oscillation that for long times evolves into the characteristic exponential decay law. By this time the coupling is essentially irreversible and reformation of the undecayed state is prohibited. As a comparison we also show the results of quantum mechanical simulations of the entire experimental sequence as solid lines in the same graph. The tunneling rates depend strongly on the well depth

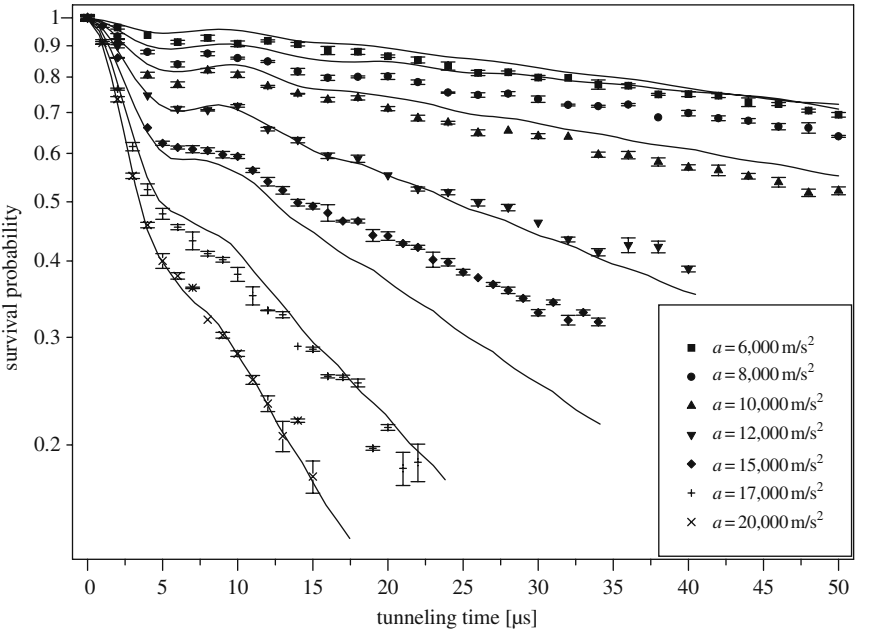

Fig. 8.12 Probability of survival in the accelerated potential as a function of duration of the tunneling acceleration. Data points for different values of the large acceleration a_{tunnel} are shown. Each point represents the average of five experimental runs, and the error bar denotes the error of the mean. These data were recorded for a well depth of $V_0/h = 92$ kHz and have been normalized to unity at $t_{\text{tunnel}} = 0$ to compare to the quantum mechanical simulations (shown in *solid lines* with no adjustable parameters)

of the potential. Considering the uncertainty of 10% in the calibration of the power in the interaction beams, the simulations match the observed data quite well.

8.5.4 Quantum Zeno and Anti-Zeno Effects

The universal phenomenon of non-exponential decay of unstable systems led Misra and Sudarshan in 1977 to the prediction that frequent measurements during this non-exponential period could inhibit decay entirely [33, 5, 41]. They named this effect the *quantum Zeno effect* after the Greek philosopher, famed for his paradoxes and puzzles. In his most famous paradox, Zeno considers an arrow flying through the air. The time of flight can be subdivided into infinitesimally small intervals during which the arrow moves only by infinitesimal amounts. Assuming the summation of infinitesimal terms amounts to nothing led Zeno to believe that motion is impossible and is merely an illusion. The version put forth by Misra and Sudarshan is the quantum mechanical version of the paradox.

To illustrate their main point, we consider the time evolution of a system in the non-exponential regime, where the probability of remaining in the undecayed

state is given by Eq. (8.45). We now subdivide the time t into n time intervals of length τ and perform a measurement of the system after each interval. Each measurement redefines a new initial condition and effectively resets the time evolution. The system must therefore start the evolution again with the same non-exponential decay features. The probability of remaining in the undecayed state at time t (after n measurements at intervals τ) is therefore $P(t) = [P(\tau)]^n$, which we can approximate as

$$P(t) = \exp\left(-n\,\tau^2 \frac{\langle H^2\rangle}{\hbar^2}\right) = e^{-\gamma t}\ , \tag{8.49}$$

where the decay rate γ is given by

$$\gamma = \tau\,\frac{\langle H^2\rangle}{\hbar^2}\ . \tag{8.50}$$

The time evolution of the system that is repeatedly measured is therefore an exponential decay. The remarkable fact is that the decay rate depends on the measurement interval τ and tends to zero as τ goes to zero. Reviews of the quantum Zeno effect can be found in modern textbooks of quantum mechanics [39]. Even though measurement-induced suppression of the dynamics of a two-state driven system has been observed [19, 24], no such effect was ever measured on an unstable system.

Whereas in the previous section we established the non-exponential time dependence, the focus of this section is the effect of measurements on the system decay rate. The quantity to be measured was the number of atoms remaining trapped in the potential during the tunneling segment. This measurement could be realized by suddenly interrupting the tunneling duration by a period of reduced acceleration a_{interr}, as indicated in Fig. 8.13(a). During this interruption tunneling was negligible and the atoms were therefore transported to a higher velocity without being lost out of the well. This separation in velocity space enabled us to distinguish the remaining atoms from the ones having tunneled out up to the point of interruption, as can be seen in Fig. 8.13(b). By switching the acceleration back to a_{tunnel}, the system was then returned to its unstable state. The measurement of the number of atoms that remained trapped defined a new initial state with the remaining number of atoms as the initial condition. The requirements for this interruption section were very similar to those during the transport section, namely the largest possible acceleration while maintaining negligible losses for atoms in the first band. Hence a_{interr} was chosen to be the same as a_{trans}.

Figure 8.14 shows the dramatic effect of frequent measurements on the decay behavior. The hollow squares indicate the decay curve without interruption. The solid circles in Fig. 8.14 depict the measurement of the survival probability in which after each tunneling segment of 1 μs an interruption of 50 μs duration was inserted. Only the short tunneling segments contribute to the total tunneling time. The survival probability clearly shows a much slower decay than the corresponding system measured without interruption. Care was taken to include the limited time response

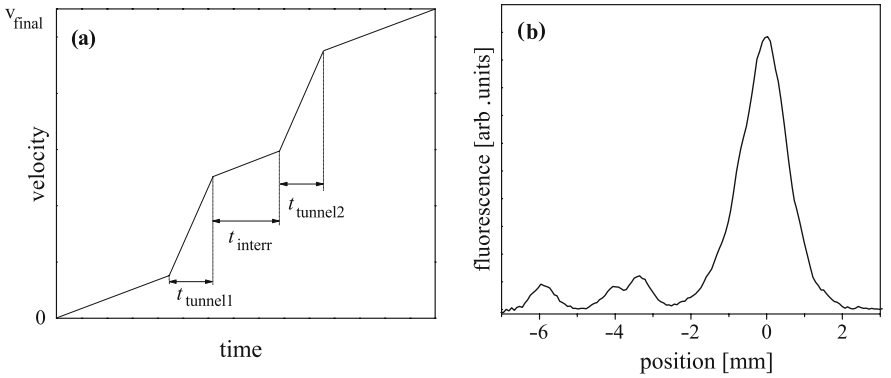

Fig. 8.13 Part (**a**) shows a diagram of the interrupted acceleration sequence. The total tunneling time is the sum of all the tunneling segments. Part (**b**) shows a typical integrated spatial distribution of atoms after ballistic expansion. The peaks can be identified as in Fig. 8.11. However, the area containing the tunneled fraction of the atoms is now composed of two peaks. Atoms that left the well during the first tunneling segment are offset in velocity from the ones having left during the second period of tunneling. The amount of separation is equal to the velocity increase of the well during the interruption. Figure from [12]; Copyright 2001 by the American Physical Society

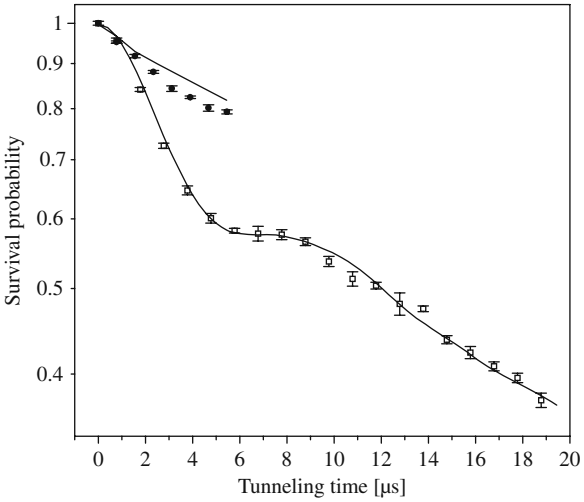

Fig. 8.14 Probability of survival in the accelerated potential as a function of duration of the tunneling acceleration. The *hollow squares* show the non-interrupted sequence, the *solid circles* show the sequence with interruptions of 50 μs duration every 1 μs. The error bars denote the error of the mean. The data have been normalized to unity at $t_{\text{tunnel}} = 0$ in order to compare to the quantum mechanical simulations (*solid lines*; no adjustable parameters). For these data the parameters were $a_{\text{tunnel}} = 15,000\ \text{m/s}^2$, $a_{\text{interr}} = 2000\ \text{m/s}^2$, $t_{\text{interr}} = 50\ \mu\text{s}$, and $V_0/h = 91$ kHz. Figure from [12]; Copyright 2001 by the American Physical Society

of the experimental setup into the analysis of the data. Also indicated as solid lines are quantum mechanical simulations of the decay by numerically integrating Schrödinger's equation for the experimental sequence and determining the survival probability numerically. The simulations contained no adjustable parameters and are in good agreement with the experimental data. We attribute the seemingly larger decay rate for the Zeno experiment as compared to the simulation to the underestimate of the actual tunneling time.

Recently it was predicted that an *enhancement* of decay can be observed for slightly longer time delays between successive measurements during the non-exponential region. In contrast to the suppressed decay for the Zeno effect this prediction was named the *anti-Zeno* effect [21, 22, 10]. The shape of the uninterrupted decay curve in Fig. 8.14 makes this suggestion fairly obvious. After an initial period of slow decay the curve shows a steep drop as part of an oscillatory feature, which for longer time damps away to show the well-known exponential decay. If the system was interrupted right after the steep drop, one would expect an overall decay that is faster than the uninterrupted decay [22]. The solid circles in Fig. 8.15 show such a decay sequence, where after every 5 μs of tunneling the decay was interrupted by a slow acceleration segment. As in the Zeno case, these interruption segments force the system to repeat the initial non-exponential decay behavior after every measurement. Here, however, the tunneling segments between the measurements are chosen longer in order to include the periods exhibiting fast

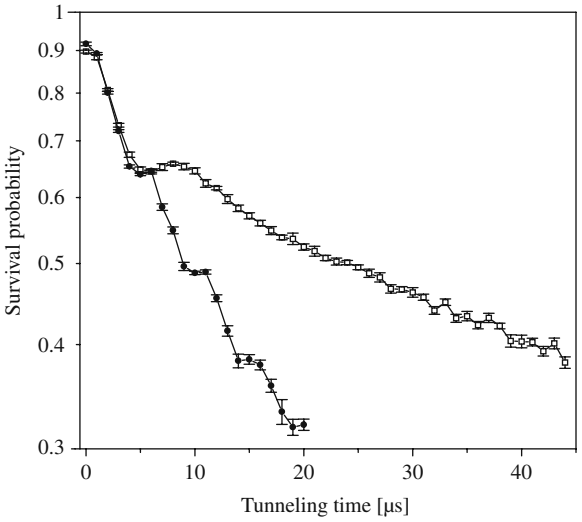

Fig. 8.15 Survival probability as a function of duration of the tunneling acceleration. The *hollow squares* show the non-interrupted sequence, the *solid circles* show the sequence with interruptions of 40 μs duration every 5 μs. The error bars denote the error of the mean. The experimental data points have been connected by *solid lines* for clarity. For these data the parameters were $a_{\text{tunnel}} = 15,000\,\text{m/s}^2$, $a_{\text{interr}} = 2800\,\text{m/s}^2$, $t_{\text{interr}} = 40\,\mu\text{s}$, and $V_0/h = 116\,\text{kHz}$. Figure from [12]; Copyright 2001 by the American Physical Society

decay. The overall decay is much faster than for the uninterrupted case, indicated by the hollow squares in the same figure.

The key to observing the Zeno and anti-Zeno effects is the ability to measure the state of the system in order to repeatedly redefine a new initial state. In our case the measurement is done by separating in momentum space the atoms still left in the unstable state from the ones that decayed into the reservoir. In order to distinguish the two classes of atoms, they must have a separation of at least the size of the momentum distribution of the unstable state, which in our case is the width of the first Brillouin zone of $\Delta p = 2\hbar k_{\mathrm{L}}$. The time it takes for an atom to be accelerated in velocity by this amount is the Bloch period $\tau_{\mathrm{B}} = 2v_{\mathrm{r}}/a_{\mathrm{interr}}$, assuming an acceleration of a_{interr}. An interruption shorter than this time will not resolve the tunneled atoms from those still trapped in the potential and therefore results in an incomplete measurement of the atom number. To investigate the effect of the interruption duration, we repeated a sequence to measure the anti-Zeno effect for varying interruption durations while holding all other parameters constant. Figure 8.16 displays the results of this measurement, interrupting the decay every 5 μs with an acceleration of a_{interr} of 2000 m/s^2. The hollow squares show the uninterrupted decay sequence as a reference. For an interruption duration smaller than the Bloch period of 30 μs, the measurement of the atom number is incomplete and has little or no effect. For a duration longer than the Bloch period, the effect saturates

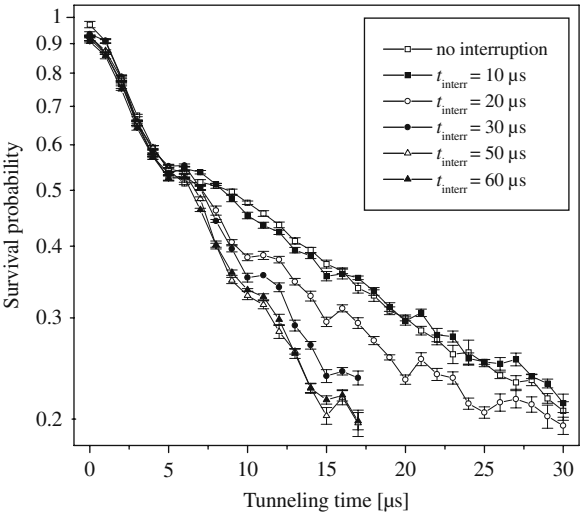

Fig. 8.16 Survival probability as a function of duration of the tunneling acceleration. The *hollow squares* show the non-interrupted sequence, other *symbols* indicate the sequence with a finite interruption duration after every 5 μs of tunneling. The error bars denote the error of the mean. A further increase of the interruption duration than as indicated does not result in a further change of the decay behavior. The experimental data points have been connected by *solid lines* for clarity. For these data the parameters were $a_{\mathrm{tunnel}} = 15,000$ m/s^2, $a_{\mathrm{interr}} = 2000$ m/s^2, and $V_0/h = 91$ kHz, leading to a Bloch period of $\tau_{\mathrm{B}} = 30$ μs. Figure from [12]; Copyright 2001 by the American Physical Society

and results in a complete restart of the decay behavior after every interruption. Even though this method of interruption is not an instantaneous measurement of the state of the unstable system, we can still accomplish the task of redefining the initial state by first switching the system from an unstable to a stable one, then in a finite time perform the measurement, and finally switching the system back to being unstable again.

8.6 Conclusions

In conclusion, we have completed a detailed study of the onset of irreversibility in an unstable quantum system and its control by repeated interrogation. We end this chapter by making some comments about possible future directions. The development of new tools to control many-body systems is a promising direction to follow. In particular, our group has been working toward the experimental realization of few-body number states [8]. These states of a definite number of atoms in the ground state of a well are an ideal starting point for the study of few-body tunneling and the onset of irreversibility. Future work in our group will focus on this problem. Finally, it is a great pleasure to acknowledge and thank the many people who have collaborated with us on this work over the years. The experiments were carried out together with Kirk Madison, Steven Wilkinson, Cyrus Bharucha, Patrick Morrow, and Braulio Gutiérrez-Medina. Theoretical work was conducted in parallel to our experiments together with Qian Niu, Roberto Diener, and Bala Sundaram. This work was supported by the R. A. Welch Foundation, the National Science Foundation, and the Sid. W. Richardson Foundation.

References

1. M. Abramowitz, I.A. Stegun (eds.), *Handbook of Mathematical Functions* (Dover, New York, 1965) 214
2. N.W. Ashcroft, N.D. Mermin, *Solid State Physics* (Saunders College, Philadelphia, 1976) 214, 217
3. C.F. Bharucha, K.W. Madison, P.R. Morrow, S.R. Wilkinson, B. Sundaram, M.G. Raizen, Phys. Rev. A **55**, R857 (1997) 227
4. F. Bloch, Z. Phys. **52**, 555 (1928) 207
5. C.B. Chiu, E.C.G. Sudarshan, B. Misra, Phys. Rev. D **16**, 520 (1977) 231
6. S. Chu, Science **253**, 861 (1991) 212
7. S. Chu, Rev. Mod. Phys. **70**, 685 (1998) 206
8. C.S. Chuu, F. Schreck, T.P. Meyrath, J.L. Hanssen, G.N. Price, M.G. Raizen, Phys. Rev. Lett. **95**, 260403 (2005) 236
9. C. Cohen-Tannoudji, J. Dupont-Roc, G. Grynberg, *Atom-Photon Interactions* (Wiley and Sons, New York, 1992) 206, 209
10. P. Facchi, H. Nakazato, S. Pascazio, Phys. Rev. Lett. **86**, 2699 (2001) 234
11. M.C. Fischer, *Atomic Motion in Optical Potentials*, Ph.D. thesis, The University of Texas at Austin (2001) 212, 214
12. M.C. Fischer, B. Gutiérrez-Medina, M.G. Raizen, Phys. Rev. Lett. **87**, 040402 (2001) 225, 230, 233, 234, 235
13. M.C. Fischer, K.W. Madison, Q. Niu, M.G. Raizen, Phys. Rev. A **58**, R2648 (1998) 223
14. L. Fonda, G.C. Ghirardi, G.C. Rimini, Rep. Prog. Phys. **41**, 587 (1978) 227, 228

15. O.R. Frisch, Z. Phys. **86**, 42 (1933) 205
16. R. Graham, M. Schlautmann, P. Zoller, Phys. Rev. A **45**, R19 (1992) 207, 208
17. P.T. Greenland, A.M. Lane, Phys. Lett. A **117**, 181 (1986) 228
18. K. Grotz, H.V. Klapdor, Phys. Rev. C **30**, 2098 (1984) 228
19. W.M. Itano, D.J. Heinzen, J.J. Bollinger, D.J. Wineland, Phys. Rev. A **41**, 2295 (1990) 232
20. L.A. Khalfin, JETP **6**, 1053 (1958) 227
21. A.G. Kofman, G. Kurizki, Phys. Rev. A **54**, R3750 (1996) 234
22. A.G. Kofman, G. Kurizki, Nature **405**, 546 (2000) 234
23. J.B. Krieger, G.J. Iafrate, Phys. Rev. B **33**, 5494 (1986) 220
24. P. Kwiat, H. Weinfurter, T. Herzog, A. Zeilinger, M. Kasevich, Phys. Rev. Lett. **74**, 4763 (1995) 232
25. R. Loudon, *The Quantum Theory of Light* (Clarendon, Oxford, 1983) 207, 208, 210
26. K.W. Madison, *Quantum Transport in Optical Lattices*, Ph.D. thesis, The University of Texas at Austin (1998) 226
27. K.W. Madison, C.F. Bharucha, P.R. Morrow, S.R. Wilkinson, Q. Niu, B. Sundaram, M.G. Raizen, Appl. Phys. B **65**, 693 (1997) 227
28. K.W. Madison, M.C. Fischer, R.B. Diener, Q. Niu, M.G. Raizen, Phys. Rev. Lett. **81**, 5093 (1998) 223
29. K.W. Madison, M.C. Fischer, M.G. Raizen, Phys. Rev. A **60**, R1767 (1999) 224
30. M.P. Marder, *Condensed Matter Physics* (Wiley and Sons, New York, 2000) 214, 217
31. E.E. Mendez, G. Bastard, Phys. Today **46**(6), 34 (1993) 207
32. P.W. Milonni, J.H. Eberly, *Lasers* (Wiley and Sons, New York, 1988) 209
33. B. Misra, E.C.G. Sudarshan, J. Math. Phys. **18**, 756 (1977) 231
34. Q. Niu, M.G. Raizen, Phys. Rev. Lett. **80**, 3491 (1998) 229
35. Q. Niu, X.G. Zhao, G.A. Georgakis, M.G. Raizen, Phys. Rev. Lett. **76**, 4504 (1996) 221, 226
36. E. Peik, M.B. Dahan, I. Bouchoule, Y. Castin, C. Salomon, Phys. Rev. A **55**, 2989 (1997) 217
37. E. Raab, M. Prentiss, A. Cable, S. Chu, D. Pritchard, Phys. Rev. Lett. **59**, 2631 (1987) 212
38. M.G. Raizen, C. Salomon, Q. Niu, Phys. Today **50**(7), 30 (1997) 207
39. J.J. Sakurai, *Modern Quantum Mechanics* (Addison-Wesley, New York, 1994) 232
40. D.A. Steck, *Sodium D Line Data (2001)*, available at http://steck.us/alkalidata 209, 210
41. P. Valanju, E.C.G. Sudarshan, C.B. Chiu, Phys. Rev. D **21**, 1304 (1980) 231
42. S.R. Wilkinson, C.F. Bharucha, M.C. Fischer, K.W. Madison, P.R. Morrow, Q. Niu, B. Sundaram, M.G. Raizen, Nature **387**, 575 (1997) 225, 229
43. R.G. Winter, Phys. Rev. **123**, 1503 (1961) 227
44. C. Zener, Proc. R. Soc. Lond. A **137**, 696 (1932) 226
45. C. Zener, Proc. R. Soc. Lond. A **145**, 523 (1934) 226